Giant Rydberg excitons in Cu_2O probed by photoluminescence excitation spectroscopy

Marijn A. M. Versteegh,[1,*] Stephan Steinhauer,[1] Josip Bajo,[1] Thomas Lettner,[1] Ariadna Soro,[1,†] Alena Romanova,[1,2] Samuel Gyger,[1] Lucas Schweickert,[1] André Mysyrowicz,[3] and Val Zwiller[1]

[1]*Department of Applied Physics, KTH Royal Institute of Technology, 106 91 Stockholm, Sweden*

[2]*Institute of Physics, Johannes Gutenberg University Mainz, 55099 Mainz, Germany*

[3]*Laboratoire d'Optique Appliquée, ENSTA, CNRS, École Polytechnique, 91762 Palaiseau, France*

(Received 25 May 2021; revised 30 November 2021; accepted 6 December 2021; published 20 December 2021)

Rydberg excitons are, with their ultrastrong mutual interactions, giant optical nonlinearities, and very high sensitivity to external fields, promising for applications in quantum sensing and nonlinear optics at the single-photon level. To design quantum applications it is necessary to know how Rydberg excitons and other excited states relax to lower-lying exciton states. Here, we present photoluminescence excitation spectroscopy as a method to probe transition probabilities from various excitonic states in cuprous oxide. We show giant Rydberg excitons at $T = 38$ mK with principal quantum numbers up to $n = 30$, corresponding to a calculated diameter of 3 μm.

DOI: 10.1103/PhysRevB.104.245206

I. INTRODUCTION

Rydberg excitons are hydrogen-atom-like bound electron-hole pairs in a semiconductor with principal quantum number $n \geqslant 2$. Rydberg excitons share common features with Rydberg atoms, which are widely studied as building blocks for emerging quantum technologies, such as quantum computing and simulation, quantum sensing, and quantum photonics [1]. Transferring Rydberg physics to the semiconductor environment offers the advantages of the well-developed semiconductor technology, opportunities for integration in microstructures, and scalability. In contrast to Rydberg atoms, which are relatively stable, Rydberg excitons have potential for ultrafast applications, since they can decay quickly. Furthermore, Rydberg excitons can serve as an interface between semiconductor physics and quantum photonics [2]. The very strong interactions between Rydberg excitons [3] and resulting giant optical nonlinearities at the single-photon level [4] are promising for applications such as single-photon emitters and single-photon transistors.

While Rydberg excitons have been observed in a few material systems [5–10], cuprous oxide (Cu_2O) takes a special position as the semiconductor capable of hosting giant Rydberg excitons with principal quantum numbers up to $n = 25$ [11], and recently even up to $n = 28$ [12]. Here, we show yellow $n = 30$ Rydberg excitons, which have an estimated diameter of 3.0 μm (for comparison, Rydberg atoms typically have diameters in the order of 100 nm) and a Rydberg blockade diameter of 23 μm [11]. In the presence of a dilute electron-hole plasma, the Rydberg exciton diameter becomes even larger due to screening effects [13,14]. Cu_2O is special in other ways as well, as it is a model semiconductor displaying all kinds of transitions (quadrupole, phonon-assisted, second class, first class) and its studies have shown to be of fundamental importance for the general understanding of exciton physics. Moreover, it is an abundant nontoxic material of which the electronic band structure allows paraexciton lifetimes in the microsecond range [15] and provides favorable conditions for Bose-Einstein condensation of excitons [16].

Yellow Rydberg excitons in Cu_2O were identified and studied in electric [17,18] and magnetic fields [19–23]. Studies of the absorption spectrum revealed quantum coherences [24] and brought an understanding of the interactions of Rydberg excitons with phonons and photons [25–27], dilute electron-hole plasma [13,14], and charged impurities [28]. Photoluminescence (PL) studies showed Rydberg states up to $n = 10$ [29], where line broadening could be explained by exciton-phonon and exciton-exciton interactions [30]. Phonon scattering from Rydberg states was studied by resonant Raman scattering spectroscopy [31] and transitions from 1*s* yellow excitons to Rydberg states by infrared Lyman spectroscopy [32,33]. Recently, theoretical studies were published on the more highly energetic green exciton series [34] and on radiative interseries transitions between Rydberg excitons [35]. An experimental paper presented signatures of coherent propagation of blue exciton polaritons [36]. Electromagnetically induced transparency may be realized for Rydberg excitations [4,37] and could enable control over exciton-phonon interactions [38]. High-quality synthetic Cu_2O microcrystals were demonstrated as host material for

*verst@kth.se

†Present address: Department of Microtechnology and Nanoscience, Chalmers University of Technology, Gothenburg, Sweden.

Published by the American Physical Society under the terms of the Creative Commons Attribution 4.0 International license. Further distribution of this work must maintain attribution to the author(s) and the published article's title, journal citation, and DOI. Funded by Bibsam.

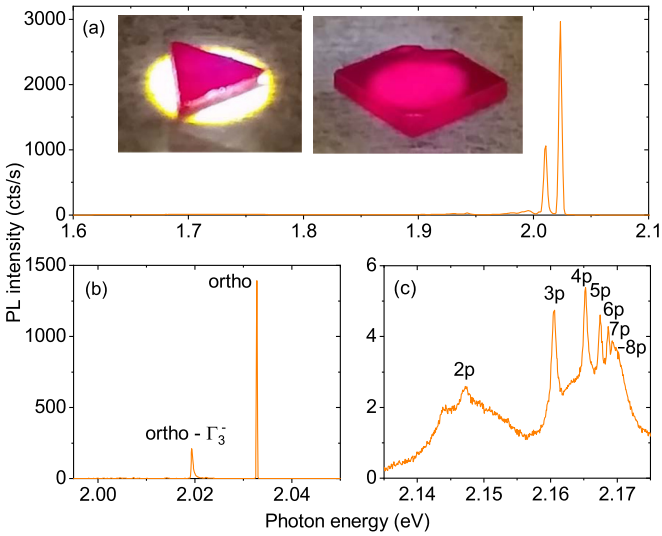

FIG. 1. Photoluminescence spectra of natural Cu_2O. (a) Yellow 1*s* orthoexciton emission and absence of defect emission at 1.7 eV. Excitation conditions: $E_{exc} = 2.17$ eV, $P = 1$ μW, $T = 170$ mK. Insets are photographs of the Tsumeb (left) and the Onganja crystal (right). (b) Zoom-in of (a), recorded with a different grating. (c) Yellow Rydberg exciton emission. Excitation conditions: $E_{exc} = 2.30$ eV, $P = 80$ μW, $T = 1.0$ K. Presented spectra are of the Tsumeb crystal; spectra of the Onganja crystal are similar.

Rydberg excitons [39], with potential for quantum confinement [40,41] and applications such as quantum sensing and single-photon emission, where the Rydberg blockade can prevent the simultaneous excitation of more than one Rydberg exciton [42].

An assessment of the opportunities of Rydberg excitons for quantum technology requires measurement of transitions to and from Rydberg states. Here, we present photoluminescence excitation (PLE) spectroscopy as a method to explore those transitions. In our approach, a PLE spectrum is constructed by scanning an excitation laser over all excitonic resonances of a Cu_2O crystal, including yellow Rydberg excitons, green and blue excitons, but excluding the yellow 1*s* excitons, from which the optical emission is recorded. Thus the PLE spectrum provides information about the transition probabilities to the 1*s* orthoexciton state. We introduce a comprehensive analytical model to describe our observations. In contrast to optical transmission spectroscopy, where one has to work with fragile thin slices of Cu_2O crystal (10-100 μm), PLE spectroscopy is also suitable on samples with large thicknesses or complex structures. It also allows studying Rydberg and other excitonic transitions in other materials, such as transition metal dichalcogenides [9].

II. EXPERIMENTAL METHODS

Experiments have been performed on two natural Cu_2O (cuprite) crystals [Fig. 1(a)]: A triangular crystal with 4 mm sides, 840-μm thick, originally from the Tsumeb mine in Namibia and part of the same specimen that was used in previous experiments [15,43,44], and a (1 0 0) oriented square with dimensions $5\times5\times1$ mm^3, purchased from Surface preparation laboratory and originally from the Onganja mine in Namibia. We observed the highest Rydberg states in the Tsumeb crystal, but in general, the two crystals show very similar behavior. Crucial for the appearance of giant Rydberg excitons is the quality of surface preparation. A polished and etched crystal was positioned inside a dilution refrigerator (Bluefors) with windows for optical measurements. The crystal lattice temperature, measured directly next to the crystal, was 38 mK at an excitation power of 2 nW. In this type of optical excitation experiments the electronic temperature is higher than the lattice temperature [45]. As excitation laser we used a tunable 1-MHz linewidth CW laser (Hübner Photonics C-Wave). Inside the dilution refrigerator, the excitation laser beam was focused by a lens ($f = 3.1$ mm, NA $= 0.70$) onto the surface of the crystal, which was mounted on top of a three-directional Attocube piezoelectric positioner stack, allowing sample alignment with respect to the laser focus with nanoscale precision. The emitted light was collected by the same lens and its spectrum was measured by a Jobin Yvon 55-cm monochromator and an Andor iDus CCD. Further details of the experimental methods are given in Appendix A.

III. EXPERIMENTAL RESULTS

PL spectra are presented in Fig. 1. The two dominant emission lines are the direct 1*s* orthoexciton quadrupole emission at 2.033 eV and the Γ_3^--phonon-assisted 1*s* orthoexciton emission at 2.020 eV. The nearly complete absence of broad emission at 1.7 eV (the maximum is 250 times lower than the direct orthoexciton emission maximum) indicates that there are almost no oxygen vacancies within the probed sample volume. When the spectrometer was tuned to the range 2.14–2.17 eV, the PL spectrum of the yellow Rydberg excitons, up to $n = 8$, was observed [Fig. 1(c)]. The low-energy shoulder of the 2*p* peak at 2.144 eV had been observed before and its origin has not yet been clarified [29].

For the construction of the PLE spectrum the excitation laser was scanned and the total count rate of the direct 1*s* orthoexciton quadrupole emission and the Γ_3^--phonon-assisted 1*s* orthoexciton emission was recorded. The measured full PLE spectrum is shown in Figs. 2(a) and 2(b). Scanning the excitation laser from low to high photon energy, the PLE signal starts at 2.047 eV with Γ_3^--phonon-assisted absorption into the yellow 1*s* orthoexciton state (simultaneous creation of an orthoexciton with $E_{1s,y,\mathrm{ortho}} = 2.0335$ eV and emission of a Γ_3^- phonon with $\hbar\omega_{\Gamma_3^-} = 13.6$ meV) [46]. At 2.116 eV the Γ_4^--phonon-assisted absorption ($\hbar\omega_{\Gamma_4^-} = 82.1$ meV) into the orthoexcitons sets in. In the range of 2.13 eV up to the yellow band gap at 2.172 eV we observe the yellow Rydberg exciton *np* resonances with well-known asymmetric Lorentzian line shapes [47]. The strong positive slope of the PLE curve in this region is caused by the start at 2.162 eV of the Γ_3^--phonon-assisted absorption into the green 1*s* orthoexciton state, in combination with the absorption into the Urbach tail of the yellow band gap. At 2.20 eV, above the yellow band gap, a maximum is reached in the PLE signal, where the mentioned phonon-assisted absorption processes are combined with absorption into the yellow continuum states. At 2.269 and 2.290 eV, the 2*p* and 3*p* green excitons respectively appear as negative peaks in the PLE signal. At 2.584 and

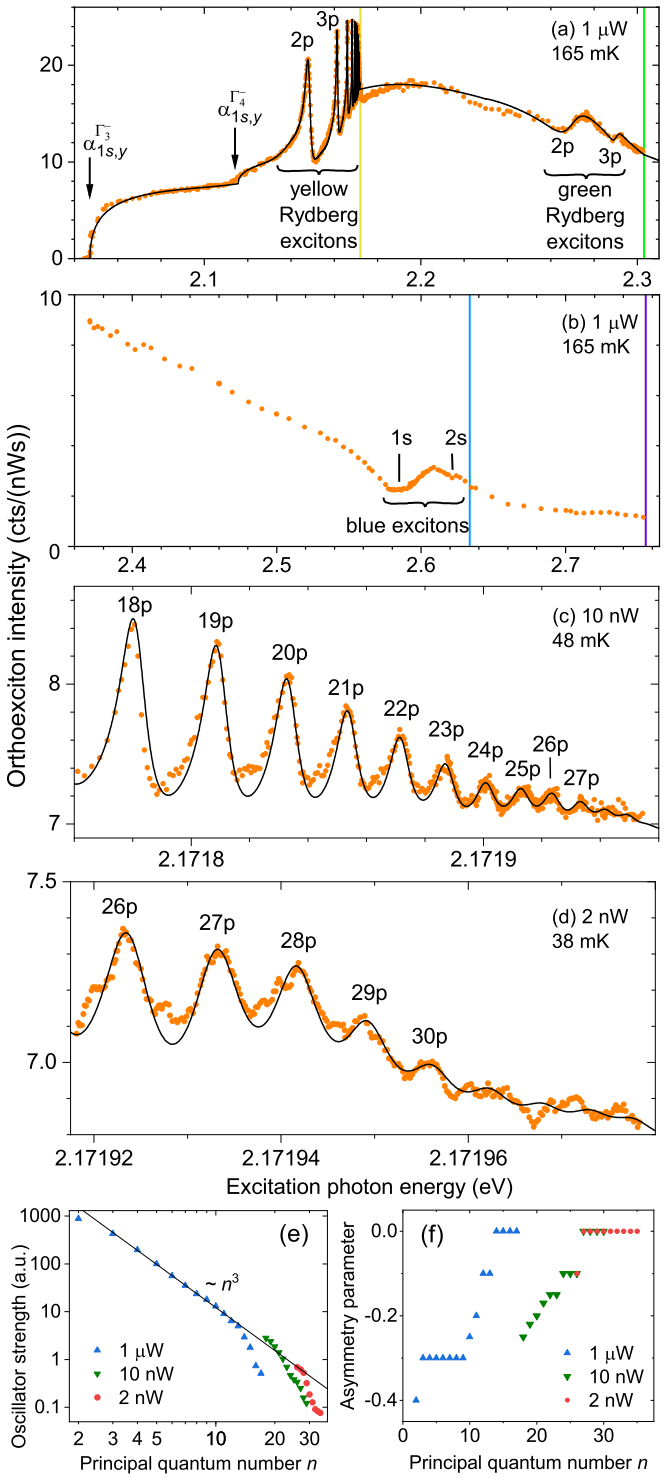

FIG. 2. Photoluminescence excitation spectra of natural Cu_2O. Detection: 1s orthoexcitons. Orange circles: experimental data. Black lines: fits. (a) Yellow Rydberg excitons (positive) and green Rydberg excitons (negative). Vertical lines indicate the yellow and green band gaps. Arrows indicate the start of the Γ_3^- and Γ_4^- phonon-assisted absorption into the yellow 1s orthoexciton state. (b) Blue excitons (negative). Vertical lines indicate the blue and indigo band gaps. Giant yellow Rydberg excitons up to (c) $n = 27$ and (d) 30. Samples are the Onganja crystal for (a) and (b) and the Tsumeb crystal for (c) and (d). (e) Oscillator strengths and (f) asymmetry parameters for the yellow np Rydberg excitons for the indicated excitation powers.

2.621 eV, we observe the 1s and 2s blue excitons as negative peaks. Indigo excitons are not visible in the PLE spectrum. The observed spectral positions of the green [34] and blue [29] excitons are consistent with literature.

Zooming in on the yellow Rydberg excitons, we observe the number of Rydberg exciton resonances increasing with decreasing excitation power [Figs. 2(c) and 2(d)], in agreement with literature [13]. At 10 nW, giant Rydberg excitons up to $n = 27$ are visible. At 2 nW, Rydberg states up to $n = 30$ can be identified, exceeding the highest Rydberg states reported so far [12]. As represented by the fitted curves, the measured Rydberg energy levels perfectly follow the Rydberg relation $\hbar\omega_n = E_{\mathrm{gap}0,y} - \mathrm{Ry}_y/(n-\delta_P)^2$, with the nominal yellow band gap $E_{\mathrm{gap}0,y} = 2.172053$ eV, the yellow Rydberg constant $\mathrm{Ry}_y = 86$ meV, and the quantum defect $\delta_P = 0.21$. The linewidths (full width at half maximum) of the Rydberg excitons are given by the relation $\Gamma_{np,y} = \Gamma_0 + \Gamma_1 n^{-3}$, where we find that $\Gamma_1 = 19$ meV and $\Gamma_0 = 5.6$ μeV at an excitation power of 2 nW and $\Gamma_0 = 7$ μeV at an excitation power of 10 nW, similar to what was observed with transmission spectroscopy [12]. The experimentally determined oscillator strengths $C_{np,y}$, presented in Fig. 2(e), are proportional to n^{-3}, but, due to the sensitivity of Rydberg excitons to charges [13], as well as to other Rydberg excitons (the Rydberg blockade effect), the oscillator strength for the high Rydberg states is lower, depending on the excitation power. The asymmetry parameters $\xi_{n,y}$ are given in Fig. 2(f). There seems to be absorption into a few Rydberg states with $n > 30$ [Fig. 2(d)], and we find that including Rydberg states up to $n = 35$ in the theoretical spectrum gives a better overall fit to the experimental data. However, Rydberg states with $n > 30$ cannot be clearly identified as the signal-to-noise ratio in this range is low and the observed maxima and minima do not follow the Rydberg relation. Decreasing the excitation power below 2 nW did not help to distinguish Rydberg states beyond $n = 30$. Features observed between the Rydberg p lines may be due to Rydberg excitons with higher orbital angular momentum [12,24].

IV. THEORY

In this section, the physical processes underlying the PLE spectroscopy are explained, as well as the shape of the PLE spectrum, which can be fitted according to the black lines in Fig. 2.

A. Optical absorption spectrum

The absorption spectrum of Cu_2O in the range of 2.0 to 2.4 eV can be written as the sum of six dominant components [26],

$$\alpha(\omega) = \alpha_{p,y} + \alpha^{\Gamma_3^-}_{1s,y} + \alpha^{\Gamma_4^-}_{1s,y} + \alpha_{p,g} + \alpha^{\Gamma_3^-}_{1s,g} + \alpha^{\Gamma_4^-}_{1s,g}, \qquad (1)$$

where $\alpha_{p,y}$ ($\alpha_{p,g}$) denotes the absorption into the yellow (green) p states, including Rydberg exciton states, continuum states, and Urbach tail, and $\alpha^{\Gamma_i^-}_{1s,y}$ ($\alpha^{\Gamma_i^-}_{1s,g}$) denotes the transition of a photon into a 1s yellow (green) orthoexciton with the simultaneous emission of a Γ_i^- phonon. The contribution of these six components and the total absorption $\alpha(\omega)$ are presented in Fig. 3(a).

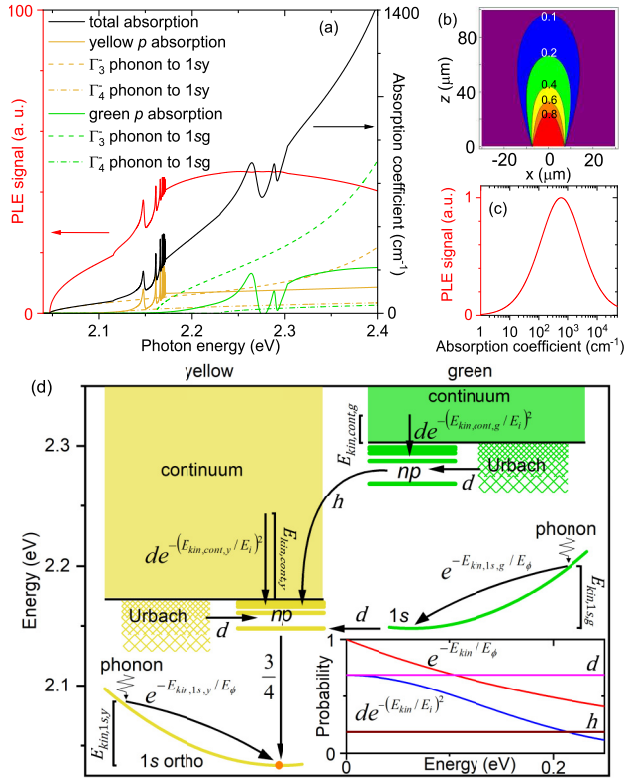

FIG. 3. Theoretical model for the photoluminescence excitation (PLE) spectrum. (a) Theoretical absorption spectrum (black) and the contributions from the dominant absorption processes (yellow and green lines). PLE spectrum according to the model where all absorbed photons create an orthoexciton with the same probability (red). (b) Relative detection probability of a photon emitted at position $(x, 0, z)$ in the crystal. (c) Relation between PLE signal and absorption coefficient in the model where all absorbed photons create an orthoexciton with the same probability. (d) Relaxation pathways from the yellow and green $1s$, np (Rydberg), continuum, and Urbach states to the thermalized yellow $1s$ orthoexciton state (orange dot) with indicated transition probabilities as inferred from the experimental data. Inset: Transition probabilities versus energy.

The absorption into yellow p states can be written as

$$\alpha_{p,y} = \alpha_{p,y,\mathrm{cont}} + \alpha_{p,y,\mathrm{Urbach}} + \sum_{n=2}^{35} \alpha_{np,y}, \tag{2}$$

where the first term describes the absorption into the continuum above the yellow gap, the second the Urbach tail, and the third the absorption into Rydberg exciton states, with asymmetric Lorentzian line shapes, where the upper limit of the summation depends on the excitation power. At 2 nW, we sum until $n = 35$ to get an optimal fit. For the absorption into green p states, we have, likewise,

$$\alpha_{p,g} = \alpha_{p,g,\mathrm{cont}} + \alpha_{p,g,\mathrm{Urbach}} + \sum_{n=2}^{3} \alpha_{np,g}. \tag{3}$$

The continuum absorption and the Urbach absorption are calculated according to the equations in Ref. [26]. The yellow Rydberg np resonances are modeled by asymmetric

TABLE I. Constants for the calculation of the absorption spectrum.

Constant	Value
$E_{\mathrm{gap},y}$ (normalized yellow band gap)	2.17196 eV (determined via PLE)
$E_{\mathrm{gap},g}$ (green band gap)	2.30302 eV [34]
$E_{1s,\mathrm{ortho}}$ ($1s$ yellow orthoexciton energy)	2.03351 eV (determined via PL)
Ry_y (yellow Rydberg constant)	86 meV [13]
$\hbar\omega_{\Gamma_3^-}$ (Γ_3^- phonon energy)	13.6 meV [46]
$\hbar\omega_{\Gamma_4^-}$ (Γ_4^- phonon energy)	82.1 meV [31]
$1s$ exciton mass	$2.61 m_0$ [48]
Yellow Bohr radius	0.81 nm [49]
Blue Bohr radius	1.72 nm [26]
$1s$ blue exciton energy	2.569 eV [26]
$2s$ blue exciton energy	2.611 eV [26]
Quadratic deformation parameter	0.168 nm^2 [26]

Lorentzians [28,47]

$$\alpha_{np,y}(\omega) = C_{np,y} \frac{\Gamma_{np,y}/2 + 2\xi_{n,y} g\left(\frac{\hbar(\omega-\omega_n)}{\Gamma_{np,y}/2}\right)\hbar(\omega-\omega_n)}{(\Gamma_{np,y}/2)^2 + \hbar^2(\omega-\omega_n)^2}, \tag{4}$$

where $C_{np,y}$ describes the oscillator strength, $\Gamma_{np,y}$ the linewidth (full width at half maximum), ω_n the resonance frequency, $\xi_{n,y}$ the asymmetry parameter, and $g(b)$ is a function included to reproduce long-range decay of symmetric Lorentzians [28] and is defined as

$$g(b) = \begin{cases} 1 & \text{if } |b| < 6; \\ e^{-\left(\frac{|b|-6}{6}\right)^2} & \text{else.} \end{cases} \tag{5}$$

We find that the parameter 6 yields an optimal fit in describing the transition between the asymmetric and the symmetric Lorentzian line shape at $3\Gamma_{np,y}$.

The constants (taken from literature) relevant to the absorption spectrum are given in Table I. The fitting parameters (obtained by fitting to the experimental data) are given in Table II. The same table also displays literature values that were used as initial values for the fitting. The PLE spectrum is not identical to the optical absorption spectrum. In fact, the relation between the absorption coefficient and the detected PLE intensity is nonmonotonic. The shape of the PLE spectrum can be understood by considering the spatial distribution of the photon absorption inside the crystal at various excitation wavelengths, the probability of decay of the various excitations into $1s$ orthoexcitons, the diffusion of those orthoexcitons through the crystal and their radiative or nonradiative decay, and finally the probability that a photon emitted by an orthoexciton is collected and detected.

B. Spatial distribution of the optical absorption

For these experiments, the front crystal surface was positioned carefully in the focal plane of the lens, which was used for both excitation and collection. From standard Gaussian optics we know that the irradiance inside the crystal of the excitation laser beam with optical angular frequency ω, in cylindrical coordinates r and z, in the presence of absorption

TABLE II. Fit parameters for the calculation of the absorption spectrum.

Fit parameter	Literature	This work
$E_{\mathrm{gap}0,y}$ (nominal yellow band gap)	2.17208 eV [11] 2.17202 eV [49]	2.172053 eV
δ_P (yel. quantum defect)	0.23 [11]	0.21
Γ_0 (minimum yellow Rydberg linewidth)	5.55 μeV [28]	5.55 μeV (2 nW) 7 μeV (10 nW)
Γ_1 (yellow Rydberg linewidth parameter)	18 meV [12]	19 meV
$C_{np,y}$ (yellow Rydberg oscillator strengths)	[11,28]	Fig. 2(e)
$\xi_{n,y}$ (Rydberg asymmetry parameters)	[11,28]	Fig. 2(f)
$E_{1s,g}$ (1s green exciton energy)	multiple energies [49]	2.148 eV
$E_{2p,g}$	2.269 eV [34]	2.269 eV
$E_{3p,g}$	2.288 eV [34]	2.290 eV
E_U (yellow and green Urbach parameter)	9.8 meV [26]	20 meV

$\alpha(\omega)$, is given by

$$I_{\mathrm{exc}}(r,z,\omega)=\frac{2P}{\pi\, w_{\mathrm{exc}}(z)^2}e^{-\frac{2r^2}{w_{\mathrm{exc}}(z)^2}-\alpha(\omega)z}. \tag{6}$$

Here, P is the power of the beam after transmission through the air-crystal interface, $w_{\mathrm{exc}}(z)=w_{\mathrm{exc},0}\sqrt{(1+(z/z_{R,\mathrm{exc}})^2}$ is the beam waist at depth z, and $z_{R,\mathrm{exc}}=\pi\, w_{\mathrm{exc},0}^2 n_{\mathrm{exc}}/\lambda_{\mathrm{exc}}$ is the Rayleigh range, with n_{exc} the index of refraction at excitation wavelength λ_{exc} and $w_{\mathrm{exc},0}=0.33$ μm the beam waist at the focus (at the front crystal surface).

The generation rate of excited states per unit of volume is given by $G(r,z,\omega)=I_{\mathrm{exc}}(r,z,\omega)\alpha(\omega)/(\hbar\omega)$. These excited states relax into orthoexcitons, with a probability depending on their state and energy. As initial model, let us assume that all excited states relax into orthoexcitons with the same probability.

C. Diffusion of orthoexcitons

Orthoexcitons have a lifetime of 3 ns [15], which is long enough to make their diffusion through the crystal non-negligible. Some orthoexcitons recombine nonradiatively at the surface and a small fraction diffuses away from the excitation beam to a part of the crystal from which the emission is not collected. Orthoexciton and paraexciton diffusion have been studied extensively [50,51]. We modeled the orthoexciton diffusion using rate equations as in Ref. [52], with a diffusion parameter of 300 cm^2/s, and with the condition that if orthoexcitons reach a surface of the crystal (only the front surface is relevant in our case) they vanish due to nonradiative recombination.

D. Detection probability

We calculate the relative detection probability for a photon emitted by a 1s orthoexciton in the Cu_2O crystal as a function of the exciton position (x,y,z). This is a common mathematical problem in microscopy [53,54]. Here, the xy plane is the front surface of the crystal, z is the depth and the focus of the lens is at (0,0,0). For a photon to be detected, it needs to be transmitted at the crystal-air interface, collected by the lens ($f=3.1$ mm, NA $=0.70$), and enter the spectrometer. A photon emitted from an exciton at the focus has the highest probability of being detected, since a wide solid angle is available for the photon to be captured, in contrast to a photon emitted deeper in the crystal. Refraction and total internal reflection at the crystal surface have to be taken into account, reducing the detection angle further. Following approaches in literature [53,54], we write the probability of detecting a photon emitted at position (x,y,z) as

$$P_{\mathrm{det}}(x,y,z)=\frac{2c_1}{\pi[w_{\mathrm{det}}(z)]^2}\int k(t,u,z)e^{\frac{-2(x-t)^2-2(y-u)^2}{[w_{\mathrm{det}}(z)]^2}}dtdu, \tag{7}$$

where c_1 is a normalization constant, $w_{\mathrm{det}}(z)=w_{\mathrm{det},0}\sqrt{1+(z/z_{R,\mathrm{det}})^2}$ is the detection waist at depth z and $z_{R,\mathrm{det}}=\pi\, w_{\mathrm{det},0}^2 n_{\mathrm{det}}/\lambda_{\mathrm{det}}$ is the detection Rayleigh range, with $n_{\mathrm{det}}=2.988$ the index of refraction at detection wavelength $\lambda_{\mathrm{det}}=610$ nm, and $w_{\mathrm{det},0}=\lambda_{\mathrm{det}}/\{\pi\tan[\arcsin(\mathrm{NA})]\}=0.20$ μm the detection waist at the focus. The function $k(t,u,z)$ is given by

$$k(t,u,z)=\begin{cases}\frac{1}{\pi[r_1(z)]^2} & \text{if } t^2+u^2\leqslant[r_1(z)]^2\\ 0 & \text{else,}\end{cases} \tag{8}$$

with $r_1(z)=r_0+zr_0/(fn_{\mathrm{det}})\approx r_0=7.3$ μm the geometrical radius of the detection area on the crystal as determined by the finite aperture stop of the detection system. The optical absorption at 610 nm in the Cu_2O crystal is negligible. The calculated relative detection probability $P_{\mathrm{det}}(x,y,z)$ is shown in Fig. 3(b), for the case of $y=0$. We find that the detection probability is almost constant from $z=0$ to $z=20$ μm, after which it decreases rapidly.

E. Photoluminescence excitation spectrum

Taking into account the shape of the excitation beam, the diffusion and surface recombination of the orthoexcitons, and the position-dependent detection probability of emitted photons, we obtain a relation between absorption coefficient and PLE signal as represented in Fig. 3(c). At low absorption coefficients, the PLE signal increases linearly, as photons emitted by orthoexcitons close to the focus have a larger probability of getting detected than photons from deep inside the crystal. However, at high absorption coefficients, the effects of diffusion and surface recombination become dominant; the PLE signal increases sublinearly, and decreases for absorption coefficients >600 cm^{-1}.

Combining this relation between the PLE signal and the absorption coefficient with the theoretical absorption spectrum, the PLE spectrum is obtained as represented by the red curve in Fig. 3(a). Comparing with the experimental data [Fig. 2(a)], it can be concluded that this model does not yet fully describe the relevant physics. For example, in the experimental spectrum the yellow Rydberg excitons have higher maxima than the above-band-gap absorption maximum at 2.20 eV, indicating that yellow Rydberg excitons have a much higher probability of decaying into a thermalized yellow

$1s$ orthoexciton than other excitations in this energy range. In addition, green excitons appear as dips in the PLE data, but they are barely visible in the red curve, because the slope of the modeled PLE signal versus absorption coefficient curve [Fig. 3(c)] is near zero in this spectral region. What therefore needs to be included in the model is a dependence of the transition probability to the thermalized $1s$ orthoexciton state on the type and energy of the photon-generated excited state.

F. Relaxation model

By fitting to the experimental data, we find transition probabilities corresponding to relaxation pathways as represented in Fig. 3(d). A physical interpretation of these transition probabilities is discussed here, first for the relaxations from the yellow states [left side of Fig. 3(d)] to the yellow $1s$ orthoexciton state [orange dot in Fig. 3(d)].

For the relaxation of yellow $1s$ orthoexcitons [created by Γ_3^- or Γ_4^- phonon-assisted absorption, illustrated in the lower left corner of Fig. 3(d)] to the thermalized $1s$ orthoexciton state (from which the emission is detected) we find a relaxation probability decaying exponentially with kinetic energy,

$$P_{1s,y}^{\Gamma_i^-}(\omega) = e^{-E_{\mathrm{kin},1s,y}/E_\phi} = e^{-(\hbar\omega - E_{1s,y,\mathrm{ortho}} - \hbar\omega_{\Gamma_i^-})/E_\phi}, \quad (9)$$

where $i = 3, 4$. For $1s$ orthoexcitons created with minimal kinetic energy, that is with photon energies $\hbar\omega$ only slightly above $E_{1s,y,\mathrm{ortho}} + \hbar\omega_{\Gamma_i^-}$, the probability of relaxation to thermalized $1s$ orthoexcitons is unity by definition. The exciton cooling process involves phonon emission, and a higher kinetic energy means a larger probability of collisions leading to dissociation or nonradiative recombination. The obtained fit parameter $E_\phi = 0.28$ eV, approximately two times the $1s$ orthoexciton binding energy, represents the exciton kinetic energy at which the probability of relaxation to the thermalized $1s$ state has dropped to $\frac{1}{e}$. The corresponding transition probability function is given as red line in the inset of Fig. 3(d).

For the yellow Rydberg excitons [from $2p$ to $35p$, indicated as np in Fig. 3(d)], we have

$$P_{np,y}(\omega) = \tfrac{3}{4}. \quad (10)$$

Yellow np Rydberg excitons relax with near-unity probability to the yellow $1s$ states via optical phonon emission [47]. The factor $3/4$ can be understood from the fact that the $1s$ orthoexciton state is a triplet state, while the $1s$ paraexciton state is a singlet state, so that three quarters of yellow Rydberg excitons decay to an orthoexciton state and one quarter of the yellow Rydberg excitons decay to a paraexciton state.

Yellow continuum states (uncorrelated electron-hole pairs) scatter via phonon emission into yellow np Rydberg states, before relaxing further into the yellow $1s$ states [31]. The transition probability from a yellow continuum state to the $1s$ orthoexciton state is therefore equal to the product of the transition probability from a yellow continuum state to a yellow np Rydberg state and the transition probability from a yellow np Rydberg state to the $1s$ orthoexciton state, which is equal to $3/4$. The fit parameter $d = 0.687$ [purple line in the inset of Fig. 3(d)] describes the probability of np-exciton formation from a low-energetic uncorrelated electron-hole pair. For higher excitations into the bands, the transition probability decreases rapidly, because energetic uncorrelated electrons and holes have a large probability of separating from each other. We find a good fit with a Gaussian function for the transition probability to the thermalized $1s$ orthoexciton state,

$$\begin{aligned} P_{p,y,\mathrm{cont}}(\omega) &= \tfrac{3}{4} d e^{-(E_{\mathrm{kin,cont,y}}/E_i)^2} \\ &= \tfrac{3}{4} d e^{-[(\hbar\omega - E_{\mathrm{gap,y}})/E_i]^2}. \end{aligned} \quad (11)$$

For the Gaussian fit parameter E_i, we obtain $E_i = 187$ meV. The continuum-to-np transition probability $d e^{-(E_{\mathrm{kin,cont,y}}/E_i)^2}$ is given as blue line in the inset of Fig. 3(d).

For the states in the yellow Urbach tail the transition probability to the $1s$ orthoexciton state is

$$P_{p,y,\mathrm{Urbach}}(\omega) = \tfrac{3}{4} d. \quad (12)$$

States in the Urbach tail can decay via phonon emission to yellow np Rydberg states, which decay further to the $1s$ orthoexciton state with probability $3/4$. Continuity at the band gap requires the inclusion of the same fit parameter d.

Now we turn to the green states [right side of Fig. 3(d)] and their relaxation to the thermalized yellow $1s$ orthoexciton state. For the Γ_3^- and Γ_4^- phonon-assisted absorption into the $1s$ green excitons (center right part of the figure) we find for the transition probability to the thermalized yellow $1s$ orthoexciton state

$$P_{1s,g}^{\Gamma_i^-}(\omega) = \tfrac{3}{4} d e^{-E_{\mathrm{kin},1s,g}/E_\phi} = \tfrac{3}{4} d e^{-(\hbar\omega - E_{1s,g} - \hbar\omega_{\Gamma_i^-})/E_\phi}, \quad (13)$$

where $i = 3, 4$. Here, we have the same exponential as in Eq. (9), describing the probability of relaxation to a low kinetic energy (given by the red line in the inset). Green $1s$ excitons strongly couple to the yellow $2p$ state [49]. The parameter d here describes the transition probability from the low-energy $1s$ green state to the yellow $2p$ state and is considered in this model to be equal to the probability of np-exciton formation from a low-energy yellow continuum state, or a yellow Urbach state. The relaxation from the yellow $2p$ state to the yellow $1s$ orthoexciton state again has probability $3/4$. The $1s$ green exciton does not have a single resonance energy, as it is, due to the strong coupling with the yellow $2p$ exciton, spread over several resonances [49]. For simplicity, however, we model a single resonance energy and obtain the best fit with $E_{1s,g} = 2.148$ eV, which is equal to $E_{2p,y}$.

For the green Rydberg excitons ($2p$ and $3p$)

$$P_{np,g}(\omega) = \tfrac{3}{4} h. \quad (14)$$

Green Rydberg excitons make a transition to a yellow continuum state, followed by decay to yellow Rydberg states, and finally to the yellow $1s$ state [31]. The probabilities of the transitions to the yellow Rydberg states are brought together into the single fit parameter h, for which we obtain $h = 0.187$ (brown line in the inset). Because of the complicated pathway, involving the transition of a hole from the Γ_8^+ to the Γ_7^+ band, h is much smaller than d.

For the continuum states above the green band gap the transition to the $1s$ orthoexciton is even more unlikely, as first the transition is to be made to one of the green Rydberg p states [31]. Similar to the transitions from the yellow continuum, we take as transition probability to the Rydberg states a factor $d e^{-(E_{\mathrm{kin,cont,y}}/E_i)^2}$ (blue line in the inset), resulting in a

total probability of transition from a green continuum state to the yellow 1*s* orthoexciton state of

$$P_{p,g,\mathrm{cont}}(\omega) = \tfrac{3}{4} h d e^{-[(\hbar\omega - E_{\mathrm{gap},g})/E_i]^2}. \quad (15)$$

For the states in the green Urbach tail, continuity at the green band gap requires that

$$P_{p,g,\mathrm{Urbach}}(\omega) = \tfrac{3}{4} h d. \quad (16)$$

G. Discussion

The full range of the fit with these transition probability functions is presented as the black curve in Fig. 2(a). The same fit is used in Figs. 2(c) and 2(d), with oscillator strengths and asymmetry parameters as given in Figs. 2(e) and 2(f). The negative shape of the green Rydberg excitons can be explained by the low probability of reaching a 1*s* yellow orthoexciton via a green Rydberg excitation, compared to the phonon-assisted yellow and green 1*s* excitations in the same energy range.

The calculation of the absorption spectrum [Fig. 3(a)] makes use of second-order perturbation theory [26], with blue excitons as virtual states, and therefore cannot be accurately extended to energies close to the blue exciton resonances. Qualitatively, the negative shape of the blue excitons [Fig. 2(b)] can be understood from the high absorption coefficient at the 1*s* and 2*s* blue exciton resonances (dipole-allowed transitions) [55], combined with the negative slope of the PLE-signal versus absorption coefficient relation at high absorption coefficients [Fig. 3(c)].

V. CONCLUSION

We presented confocal PLE spectroscopy as a method to measure a variety of optical excitations in Cu_2O: Yellow and green Rydberg excitons, blue excitons, yellow and green continuum and Urbach states, as well as phonon-assisted absorption into excitonic states. A quantitative analysis of the spectroscopic method is given. Since the optical emission from the yellow 1*s* orthoexcitons was detected, the observed PLE spectrum reveals information about the transition probabilities from the various excitations to the yellow 1*s* orthoexciton state. A model for these transition probabilities is presented, which can be used as input into theoretical calculations to obtain a deeper understanding of the excitonic transitions and interactions in Cu_2O. By PLE spectroscopy on a well-polished and etched crystal in a dilution refrigerator, we have been able to identify giant yellow Rydberg *p* excitons up to $n = 30$, corresponding to a diameter of 3.0 μm and a blockade diameter of 23 μm [11]. The observation of these high Rydberg states is important, since all nonlinearities scale drastically with n (the van der Waals interaction coefficient scales with n^{11} [3]), and therefore the discovery of these new Rydberg states increases possibilities for applications in quantum technology [4]. Interestingly, a recent theoretical paper predicts dominance of radiative transitions and appearance of polaritonic features for $n > 28$ [27], which opens up exciting opportunities for future studies.

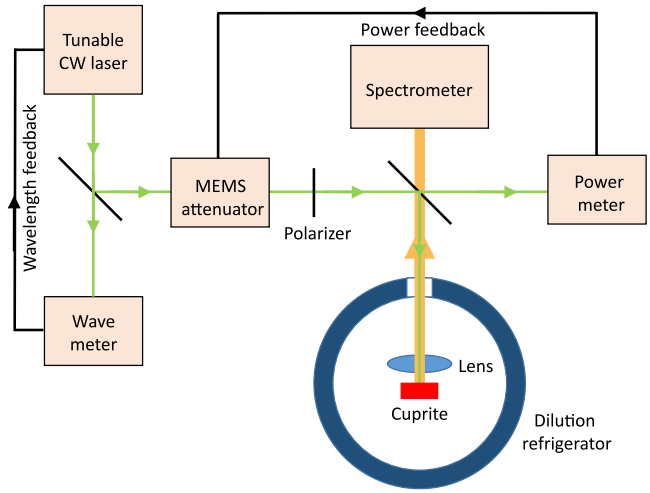

FIG. 4. Schematic of the experimental setup.

ACKNOWLEDGMENTS

We thank D. Fröhlich for his advice on sample preparation. We acknowledge support from the Swedish Research Council (Starting Grants No. 2016-04527 and No. 2019-04821) and from the Göran Gustafsson Foundation.

APPENDIX A: EXPERIMENTAL METHODS

1. Sample preparation

Before measurement, the Cu_2O crystals were carefully polished using MicroCloth and an alkaline colloidal silica polishing solution (Ludox), until a mirror-like surface was obtained and even micrometer-sized dips at the surface had disappeared. After polishing, the crystals were etched using hydrochloric acid (HCl) and ammonia (NH_3) [29]. First, a polished crystal was held for 10 s in the HCl solution (2 mol/l), then rinsed with distilled water and blown dry with N_2. Second, the crystal was held for 10 s in ammonia (13 mol/l), then rinsed with water and blown dry with N_2. At this point, the crystal had an opaque appearance with blue/grey color. After carefully removing loose material from the surface with a wet foam head swap (Texwipe), the crystal retained its transparency. This etching procedure was repeated two more times. The quality of surface preparation was crucial for the appearance of giant Rydberg excitons. Polishing with the colloidal silica solution gave the best polishing result, and this, in turn, resulted in the observation of the highest Rydberg states. Surface charges have a detrimental effect on giant Rydberg excitons, because of the Stark effect [12,28]. In order to minimize oxidation, we mounted the cuprite crystal directly after etching in the dilution refrigerator, which was immediately evacuated. In vacuum, the crystal quality can be maintained at least for several months. We have observed that when the crystal is kept in air for several days, however, defect emission appears in the PL spectrum and the highest Rydberg excitons are no longer observed. The original spectrum can then be recovered by careful polishing and etching of the surface.

2. Laser stabilization

A schematic of the setup is given in Fig. 4. As excitation laser we used a tunable 1-MHz linewidth CW laser (Hübner Photonics C-Wave). The laser frequency was stabilized to within 10 MHz (or 40 neV), using a HighFinesse wavemeter and a feedback mechanism (called AbsoluteLambda) in the C-Wave laser.

The laser power was stabilized to within 0.1% using a MEMS fiber-optic attenuator. The input power of the excitation laser was attenuated using a MEMS based variable attenuator (Thorlabs, V450A). In front of the dilution refrigerator a plate beam splitter was placed, which reflected 10% of the laser power into the dilution refrigerator and transmitted 90% of the optical signal from the Cu_2O crystal towards the spectrometer. The 90% of the laser power transmitted by this plate beam splitter was sent to a power meter (Thorlabs PM100USB with S120C Powerhead). The splitting ratio was calibrated using a handheld power meter. The measured power was used as set point in a software controlled PID controller (LabVIEW). The generated control signal was sent to a homebuild Digital Analog Converter based on an DAC-IC (AD5541A, Analog Devices) controlled by an ESP32 Feather board (Adafruit). With this setup, the power fluctuations were smaller than 0.1%.

For the PLE spectrum taken with a wide spectral range [Figs. 2(a) and 2(b)], the laser focus was carefully adjusted during the scan to ensure that is was always at the crystal surface. For the PLE spectra taken with a small spectral range [Figs. 2(c) and 2(d)], no such adjustment was needed.

3. Construction of the PLE spectrum

For the construction of the PLE spectrum, the excitation laser was scanned with step sizes ranging from 0.2 μeV in the region with the highest Rydberg states to a few meV in spectral regions far away from any resonances. The emitted light was measured by a Jobin Yvon 55-cm monochromator and an Andor iDus CCD. The total count rate of the two dominant $1s$ orthoexciton emission lines, namely the direct $1s$ orthoexciton quadrupole emission at 2.033 eV and the Γ_3^--phonon-assisted $1s$ orthoexciton emission at 2.020 eV [Fig. 1(b)] was recorded for each step, with integration times between 15 s and 200 s, depending on the chosen excitation power. At the lowest excitation power of 2 nW, where an integration time of 200 s per step was used, a sliding average was calculated of 7 subsequent steps, in order to reduce the noise.

In the raw PLE data, a sinusoidal oscillation is visible with a constant period of 73 μeV and an amplitude of 0.16 cts/(nWs). This oscillation is visible both in the spectral region with the yellow Rydberg excitons and in the spectral regions below the yellow $2p$ state and above the yellow band gap, and is presumably the result of an optical interference in our setup. In order to address this effect, we subtracted the function $A\cos[\frac{2\pi}{B}(\hbar\omega - C)]$, with $A = 0.16$ cts/(nWs), $B = 73$ μeV, and $C = 2.171765$ eV from the raw data and presented the corrected data in Figs. 2(c) and 2(d). Note that the period of these oscillations is much larger than the separation between two adjacent giant Rydberg exciton levels.

[1] C. S. Adams, J. D. Pritchard, and J. P. Shaffer, Rydberg atom quantum technologies, J. Phys. B: At. Mol. Opt. Phys. **53**, 012002 (2020).

[2] M. Assmann and M. Bayer, Semiconductor Rydberg physics, Adv. Quantum Technol. **3**, 1900134 (2020).

[3] V. Walther, S. O. Krüger, S. Scheel, and T. Pohl, Interactions between Rydberg excitons in Cu_2O, Phys. Rev. B **98**, 165201 (2018).

[4] V. Walther, R. Johne, and T. Pohl, Giant optical nonlinearities from Rydberg excitons in semiconductor microcavities, Nat. Commun. **9**, 1309 (2018).

[5] E. F. Gross, Optical spectrum of excitons in the crystal lattice, Nuovo Cimento **3**, 672 (1956).

[6] V. T. Agekyan, Spectroscopic properties of semiconductor crystals with direct forbidden energy gap, Phys. Stat. Solidi (a) **43**, 11 (1977).

[7] A. Chernikov, T. C. Berkelbach, H. M. Hill, A. Rigosi, Y. Li, O. B. Aslan, D. R. Reichman, M. S. Hybertsen, and T. F. Heinz, Exciton Binding Energy and Nonhydrogenic Rydberg Series in Monolayer WS_2, Phys. Rev. Lett. **113**, 076802 (2014).

[8] K. He, N. Kumar, L. Zhao, Z. Wang, K. F. Mak, H. Zhao, and J. Shan, Tightly Bound Excitons In Monolayer WSe_2, Phys. Rev. Lett. **113**, 026803 (2014).

[9] H. M. Hill, A. F. Rigosi, C. Roquelet, A. Chernikov, T. C. Berkelbach, D. R. Reichman, M. S. Hybertsen, L. E. Brus, and T. F. Heinz, Observation of excitonic Rydberg states in monolayer MoS_2 and WS_2 by photoluminescence excitation spectroscopy, Nano Lett. **15**, 2992 (2015).

[10] T. Wang, Z. Li, Y. Li, Z. Lu, S. Miao, Z. Lian, Y. Meng, M. Blei, T. Taniguchi, K. Watanabe, S. Tongay, D. Smirnov, C. Zhang, and S. F. Shi, Giant valley-polarized rydberg exciton in monolayer WSe_2 revealed by magneto-photocurrent spectroscopy, Nano Lett. **20**, 7635 (2020).

[11] T. Kazimierczuk, D. Fröhlich, S. Scheel, H. Stolz, and M. Bayer, Giant Rydberg excitons in the copper oxide Cu_2O, Nature (London) **514**, 343 (2014).

[12] J. Heckötter, D. Janas, R. Schwartz, M. Assmann, and M. Bayer, Experimental limitation in extending the exciton series in Cu_2O towards higher principal quantum numbers, Phys. Rev. B **101**, 235207 (2020).

[13] J. Heckötter, M. Freitag, D. Fröhlich, M. Assmann, M. Bayer, P. Grünwald, F. Schöne, D. Semkat, H. Stolz, and S. Scheel, Rydberg Excitons in the Presence of an Ultralow-Density Electron-Hole Plasma, Phys. Rev. Lett. **121**, 097401 (2018).

[14] V. Walther and T. Pohl, Plasma-Enhanced Interaction and Optical Nonlinearities of Cu_2O Rydberg Excitons, Phys. Rev. Lett. **125**, 097401 (2020).

[15] A. Mysyrowicz, D. Hulin, and A. Antonetti, Long Exciton Lifetime in Cu_2O, Phys. Rev. Lett. **43**, 1123 (1979).

[16] D. Snoke and G. M. Kavoulakis, Bose-Einstein condensation of excitons in Cu_2O: progress over 30 years, Rep. Prog. Phys. **77**, 116501 (2014).

[17] J. Heckötter, M. Freitag, D. Fröhlich, M. Assmann, M. Bayer, M. A. Semina, and M. M. Glazov, High-resolution study of the yellow excitons in Cu_2O subject to an electric field, Phys. Rev. B **95**, 035210 (2017).

[18] J. Heckötter, M. Freitag, D. Fröhlich, M. Assmann, M. Bayer, M. A. Semina, and M. M. Glazov, Dissociation of excitons in Cu_2O by an electric field, Phys. Rev. B **98**, 035150 (2018).

[19] M. Assmann, J. Thewes, D. Fröhlich, and M. Bayer, Quantum chaos and breaking of all antiunitary symmetries in Rydberg excitons, Nat. Mater. **15**, 741 (2016).

[20] J. Heckötter, M. Freitag, D. Fröhlich, M. Assmann, M. Bayer, M. A. Semina, and M. M. Glazov, Scaling laws of Rydberg excitons, Phys. Rev. B **96**, 125142 (2017).

[21] S. Zielinska-Raczynska, D. Ziemkiewicz, and G. Czajkowski, Magneto-optical properties of Rydberg excitons: Center-of-mass quantization approach, Phys. Rev. B **95**, 075204 (2017).

[22] S. Artyukhin, D. Fishman, C. Faugeras, M. Potemski, A. Revcolevschi, M. Mostovoy, and P. H. M. van Loosdrecht, Magneto-absorption spectra of hydrogen-like yellow exciton series in cuprous oxide: excitons in strong magnetic fields, Sci. Rep. **8**, 7818 (2018).

[23] A. Farenbruch, D. Fröhlich, D. R. Yakovlev, and M. Bayer, Rydberg Series of Dark Excitons in Cu_2O, Phys. Rev. Lett. **125**, 207402 (2020).

[24] P. Grünwald, M. Assmann, J. Heckötter, D. Fröhlich, M. Bayer, H. Stolz, and S. Scheel, Signatures of Quantum Coherences in Rydberg Excitons, Phys. Rev. Lett. **117**, 133003 (2016).

[25] F. Schweiner, J. Main, and G. Wunner, Linewidths in excitonic absorption spectra of cuprous oxide, Phys. Rev. B **93**, 085203 (2016).

[26] F. Schöne, H. Stolz, and N. Naka, Phonon-assisted absorption of excitons in Cu_2O, Phys. Rev. B **96**, 115207 (2017).

[27] H. Stolz, F. Schöne, and D. Semkat, Interaction of Rydberg excitons in cuprous oxide with phonons and photons: optical linewidth and polariton effect, New J. Phys. **20**, 023019 (2018).

[28] S. O. Krüger, H. Stolz, and S. Scheel, Interaction of charged impurities and Rydberg excitons in cuprous oxide, Phys. Rev. B **101**, 235204 (2020).

[29] M. Takahata and N. Naka, Photoluminescence properties of the entire excitonic series in Cu_2O, Phys. Rev. B **98**, 195205 (2018).

[30] T. Kitamura, M. Takahata, and N. Naka, Quantum number dependence of the photoluminescence broadening of excitonic Rydberg states in cuprous oxide, J. Lumin. **192**, 808 (2017).

[31] P. Y. Yu and Y. R. Shen, Resonance Raman studies in Cu_2O. II. The yellow and green excitonic series, Phys. Rev. B **17**, 4017 (1978).

[32] E. T. E. Jörger, T. Fleck, and C. Klingshirn, Infrared absorption by excitons in Cu_2O, Phys. stat. sol. (b) **238**, 470 (2003).

[33] K. Yoshioka, T. Ideguchi, and M. Kuwata-Gonokami, Laser-based continuous-wave excitonic Lyman spectroscopy in Cu_2O, Phys. Rev. B **76**, 033204 (2007).

[34] P. Rommel, P. Zielinski, and J. Main, Green exciton series in cuprous oxide, Phys. Rev. B **101**, 075208 (2020).

[35] S. O. Krüger and S. Scheel, Interseries transitions between Rydberg excitons in Cu_2O, Phys. Rev. B **100**, 085201 (2019).

[36] J. Schmutzler, D. Fröhlich, and M. Bayer, Signatures of coherent propagation of blue polaritons in Cu_2O, Phys. Rev. B **87**, 245202 (2013).

[37] D. Ziemkiewicz, Electromagnetically induced transparency in media with Rydberg excitons 1: Slow light, Entropy **22**, 177 (2020).

[38] V. Walther, P. Grünwald, and T. Pohl, Controlling Exciton-Phonon Interactions via Electromagnetically Induced Transparency, Phys. Rev. Lett. **125**, 173601 (2020).

[39] S. Steinhauer, M. A. M. Versteegh, S. Gyger, A. W. Elshaari, B. Kunert, A. Mysyrowicz, and V. Zwiller, Rydberg excitons in Cu_2O microcrystals grown on a silicon platform, Comm. Mater. **1**, 11 (2020).

[40] A. Konzelmann, B. Frank, and H. Giessen, Quantum confined Rydberg excitons in reduced dimensions, J. Phys. B: At. Mol. Opt. Phys. **53**, 024001 (2020).

[41] K. Orfanakis, S. K. Rajendran, H. Ohadi, S. Zielińska-Raczyńska, G. Czajkowski, K. Karpiński, and D. Ziemkiewicz, Quantum confined Rydberg excitons in Cu_2O nanoparticles, Phys. Rev. B **103**, 245426 (2021).

[42] M. Khazali, K. Heshami, and C. Simon, Single-photon source based on Rydberg exciton blockade, J. Phys. B: At. Mol. Opt. Phys. **50**, 215301 (2017).

[43] D. Snoke, J. P. Wolfe, and A. Mysyrowicz, Quantum Saturation of a Bose Gas: Excitons in Cu_2O, Phys. Rev. Lett. **59**, 827 (1987).

[44] D. W. Snoke, J. P. Wolfe, and A. Mysyrowicz, Evidence for Bose-Einstein Condensation of a Two-Component Exciton Gas, Phys. Rev. Lett. **64**, 2543 (1990).

[45] K Yoshioka, Y. Morita, K. Fukuoka, and M. Kuwata-Gonokami, Generation of ultracold paraexcitons in cuprous oxide: A path toward a stable Bose-Einstein condensate, Phys. Rev. B **88**, 041201(R) (2013).

[46] P. Y. Yu and Y. R. Shen, Resonance Raman studies in Cu_2O. I. The phonon-assisted 1s yellow excitonic absorption edge, Phys. Rev. B **12**, 1377 (1975).

[47] Y. Toyozawa, Interband effect of lattice vibrations in the exciton absorption spectra, J. Phys. Chem. Solids. **25**, 59 (1964).

[48] J. Brandt, D. Fröhlich, C. Sandfort, M. Bayer, H. Stolz, and N. Naka, Ultranarrow Optical Absorption and Two-Phonon Excitation Spectroscopy of Cu_2O Paraexcitons in a High Magnetic Field, Phys. Rev. Lett. **99**, 217403 (2007).

[49] F. Schweiner, J. Main, G. Wunner, and C. Uihlein, Even exciton series in Cu_2O, Phys. Rev. B **95**, 195201 (2017).

[50] D. P. Trauernicht and J. P. Wolfe, Drift and diffusion of paraexcitons in Cu_2O: Deformation-potential scattering in the low-temperature regime, Phys. Rev. B **33**, 8506 (1986).

[51] Y. Morita, H. Suzuki, K. Yoshioka, and M. Kuwata-Gonokami, Observation of ultrahigh mobility excitons in a strain field by space- and time-resolved spectroscopy at subkelvin temperatures, Phys. Rev. B **100**, 035206 (2019).

[52] K. Yoshioka, T. Ideguchi, A. Mysyrowicz, and M. Kuwata-Gonokami, Quantum inelastic collisions between paraexcitons in Cu_2O, Phys. Rev. B **82**, 041201(R) (2010).

[53] R. H. Webb, Confocal optical microscopy, Rep. Prog. Phys. **59**, 427 (1996).

[54] K. Ahi, Mathematical modeling of THz point spread function and simulation of THz imaging systems, IEEE Trans. THz Sci. Technol. **7**, 747 (2017).

[55] A. Daunois, J. L. Deiss, and B. Meyer, Étude spectrophotométrique de l'absorption bleue et violette de Cu_2O, J. Phys. **27**, 142 (1966).